1.8 MeV PROTON RESPONSE OF THERMALLY STABILIZED GALLIUM NITRIDE RF POWER TRANSISTORS

By

Michael W. A. McCurdy

Thesis
Submitted to the Faculty of the
Graduate School of Vanderbilt University
in partial fulfillment of the requirements
for the degree of

MASTER OF SCIENCE
in

Electrical Engineering
December 16, 2017
Nashville, Tennessee

Approved:

Ronald D. Schrimpf, Ph.D.

Daniel M. Fleetwood, Ph.D.

ACKNOWLEDGMENTS

I am exceedingly grateful for the support and encouragement of my advisor, Dr. Ron Schrimpf. If it weren't for him I would not have completed this. I also thank Drs. Dan Fleetwood, Robert Reed, Marcus Mendenhall, Art Witulski and Robert Weller for helpful technical discussions. Thanks to Ken Bole and Brian Poling of AFRL for helpful discussion and input on this effort. Thanks are also due to Drs. Andrew Sternberg and En Xia Zhang for their help and input with many testing related efforts. I would also like to thank the many RER students I have worked with on research and testing efforts over the last 13 years.

Tremendous gratitude goes to my wonderful wife, Kathy, for unending support and encouragement, and to our children Hannah and Caleb, who are a constant source of joy and pride.

Thanks go to the Air Force Research Laboratory for providing hardware and financial support for this effort.

TABLE OF CONTENTS

Page

ACKNOWLEDGMENTS ii

LIST OF TABLES iv

LIST OF FIGURES v

Chapter

1. Introduction 1

2. Background 3

    Semiconductors 3
    Radiation Damage 8

3. Test Setup 10

    Devices 10
    Thermoelectric Cooling 11
    Test Equipment and Protocol 13
    S-parameters and the Smith Chart 17

4. Results 20

    DC Parameters 20
    Small Signal RF 24
    Large Signal RF 28

5. Conclusions 31

REFERENCES 33

LIST OF TABLES

Table Page

2.1 Semiconductor properties at 300 K....6

3.1 Device and operational mode specs....10

3.2 TE system components....11

3.3 List of equipment....13

3.4 Irradiation fluence steps....15

LIST OF FIGURES

Figure Page

2.1 Silicon n-channel MOSFET energy band diagrams 4

2.2 Basic AlGaN/GaN transistor cross section 7

2.3 AlGaN/GaN polarization components and energy band diagram 8

2.4 Bragg curve for 1.8 MeV protons in GaN 9

3.1. Device photos....11

3.2 Thermoelectric system....12

3.3 EVB shield....14

3.4 Test equipment setup 16

3.5 Two-port network topology 17

3.6 Simplified Smith Chart 19

4.1 I_D-V_G Curves for C4 (SO) showing V_{TH} and g_m 21

4.2. Maximum V_{TH} shift and g_m degradation 21

4.3 V_{TH} shift for all operational modes 22

4.4 CGH40120F (FO) V_{TH} shift 23

4.5 C4 and C10 (SO) g_m degradation....24

4.6 Typical g_m degradation for devices....25

4.7 *S21* response of C4 (SO) and R8 (RF)....26

4.8 *S21* response of T15 (RF) and *S11* response of T15 and T16 (RF)....27

4.9 T11 (SO) S-parameter sweeps pre-irradiation and post-rad 29

4.10 RF large signal gain, worst case 30

CHAPTER 1

INTRODUCTION

Aluminum gallium nitride/gallium nitride ($Al_xGa_{1-x}N$/GaN), hereinafter referred to as AlGaN/GaN for simplicity, high electron mobility transistors (HEMTs) are experiencing widespread use in RF, and growing use in power electronics, applications. High speed, high frequency, and high power operation due to wide band gap, high carrier mobility, high saturation velocity, high temperature operation, excellent thermal properties, and high breakdown voltage make AlGaN/GaN extremely attractive for a variety of applications in harsh environments like space. The direct band gap allows optoelectronics functions.

GaN-based HEMTs are deployed in RF applications from low power cell phone and radio functions to high power radar and satellite communications. Use of commercial off the shelf (COTS) parts has become commonplace where high reliability and/or radiation hardened parts are not available. Proper testing of COTS parts informs circuit design and mitigation techniques so that such parts can be adapted for use in harsh environments. The Air Force Research Laboratory provided COTS RF power AlGaN/GaN HEMTs from three different manufacturers to test their response to 1.8 MeV protons. This document describes that study. The content that follows starts with fundamental device physics in Chapter 2. We begin with silicon because of its ubiquity, and then cover GaN-based HEMTs and discuss the significant differences. In Chapter 3 we discuss specifics of the three device types, details of the thermoelectric cooling system components and assembly, electrical test equipment used and the test protocol. An introduction to S-parameters and the Smith chart is also included. Chapter 4

covers the test results, the most surprising of which that was all TriQuint parts exhibited increased small signal RF gain with increasing fluence. This was not seen in any other parts. The Cree devices exhibited lowest overall sensitivity to 1.8 MeV protons. We conclude with Chapter 5, suggesting that a carefully planned comprehensive test protocol should be used to vet AlGaN/GaN HEMT RF power devices for critical applications. The number of process variables encountered over the many manufacturers and the technology evolution rate of change dictate such an approach.

CHAPTER 2

BACKGROUND

Semiconductors

A semiconductor's properties are determined by the electronic energy band structure that arises from the constituent atoms arrayed in a crystal lattice. The constituents' valence state, determined by the periodic table group (column) they occupy, and type of crystal lattice influence this. The gap between the electron conduction and valence bands will determine the material's breakdown voltage and the intrinsic carrier concentration. The lattice sets up periodic potentials that the charge carriers experience as they move through the lattice, which determine the wave functions and transport properties. Most semiconductors are anisotropic in that the lattice spacings and carrier transport characteristics are different along different crystal directions. Thus, charge carriers experience different conditions and exhibit different conduction characteristics depending on their direction of travel in the crystal. Complex energy-momentum (E-p, or E-k) diagrams help show this phenomenon. Because of this anisotropy, semiconductors are fabricated with a known crystal orientation to maximize operational characteristics [1][2][3].

Silicon is a quadrivalent (group IV) semiconductor and has the diamond cubic lattice structure. It is commonly doped with pentavalent (group V) elements phosphorus or arsenic, called *donors* since they donate an unbound electron, to make n-type semiconductor. Similarly, silicon is commonly doped with trivalent group III elements boron or aluminum, called *acceptors* since they introduce a bond site vacancy, or hole, that may accept an electron, to make p-type semiconductor. The donors and acceptors make up the bulk of the charge carriers. In a

silicon metal-oxide-semiconductor field effect transistor (MOSFET) the channel is formed and manipulated by applying voltages to the gate and drain terminals while the source is typically grounded. These applied voltages change the energy band structure so that minority carriers can form an inversion-layer (channel) due to the gate voltage, and can create a current due to the drain voltage. Fig. 2-1 shows the band diagrams for four n-channel transistor bias conditions.

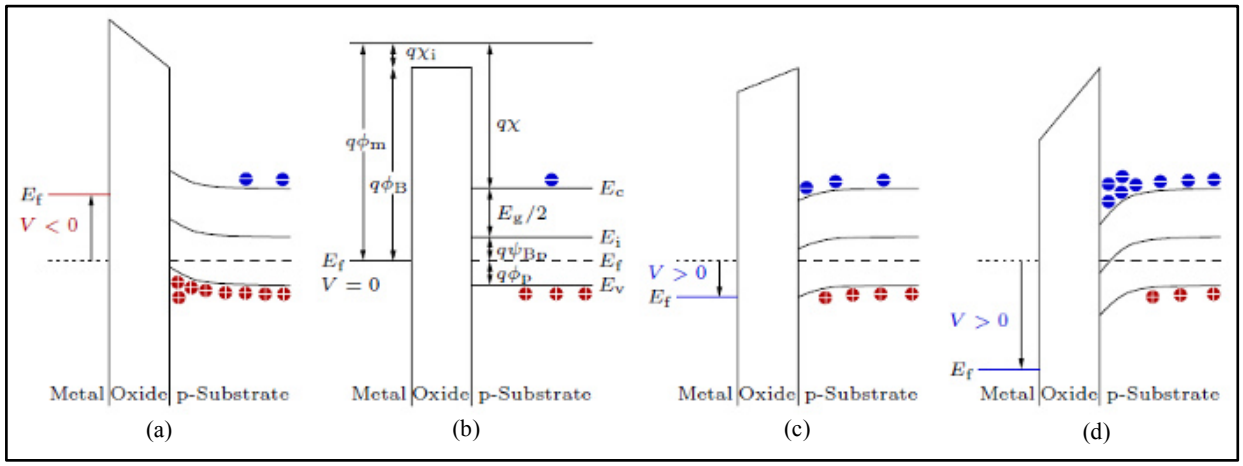

Fig. 2.1. Silicon n-channel MOSFET energy band diagrams - (a) accumulation, (b) flatband, (c) depletion, (d) inversion [4].

Accumulation is shown in Fig. 2-1 (a). This is the *off* condition where the majority carriers of the substrate accumulate under the gate oxide. The gate is well below the threshold voltage, V_{TH}, for this condition and can be negative. V represents the gate voltage in the Figure. The drain is biased at a nominal positive value. In Fig. 2-1(b), (c) and (d) the gate voltage increases monotonically from that of accumulation mode. The transistor is being turned more to the *on* state as it goes through flatband, depletion, and lastly, inversion. *Flatband* is self-descriptive and means the energy bands are flat. The term *depletion* indicates the channel region is depleted of carriers, i.e., p and n are both small compared to the equilibrium majority-carrier density. The

term *inversion* indicates the formed channel consists of minority carriers (electrons) in the p-type substrate, i.e., $n >> p$, and the device is fully on.

GaN is a binary semiconductor, since it is comprised of gallium, a group III element, and nitrogen, a group V element. GaN may form zincblende cubic or wurtzite hexagonal crystal structures. The wurtzitic form is the most thermodynamically stable and is used to make devices. It also has a larger band gap: 3.4 eV for wurtzite vs. 3.2 eV for zincblende. AlN and InN are also important commonly employed semiconductors with all the properties previously mentioned for GaN except for the band gap values. GaN, AlN and InN may be combined in ternary and quaternary forms to make semiconductors with a spectrum of various properties. $Al_xGa_{1-x}N$ (AlGaN hereinafter for simplicity) is a ternary semiconductor with the stoichiometric proportions of Al and Ga determined by x, and is also used in the wurtzitic form. AlN has a band gap of 6.2 eV. AlGaN has a band gap that scales from 3.42 eV (GaN) to 6.2 eV (AlN) depending on x, thus AlGaN has a larger band gap than GaN. To make a GaN HEMT a thin layer of AlGaN, called a barrier layer, is grown on top of a GaN base, where x is typically 0.25 to 0.30 although devices can be found employing much higher values. Fabrication processes vary, and may employ metal organic chemical vapor deposition (MOCVD) or plasma assisted molecular beam epitaxy (PAMBE) growth under Ga-rich or NH_3-rich conditions on SiC or GaN substrates. AlGaN has a slightly smaller lattice constant than GaN so it is under tensile stress. Many wurtzitic materials exhibit piezoelectric properties with AlGaN and GaN being no exception. In the AlGaN there is a large spontaneous polarization due to the crystal orientation and a piezoelectric polarization that manifests due to the tensile stress. In addition, a spontaneous polarization exists in the GaN. The polarization effects, along with the band gap difference-induced electric field, cause band bending such that the conduction band dips below the Fermi level in the GaN just below the

heterojunction. This creates a quantum well that fills with electrons from the AlGaN, forming a thin layer with a high concentration of high mobility carriers called a 2-dimensional electron gas (2-DEG) [3][5][6][7]. A number of properties of interest for several semiconductors are shown in Table 2-1.

Table 2.1. Semiconductor properties at 300 K.

Quantity	Symbol	Si	Ge	GaAs	GaN	AlN	Units
Crystal structure	–	Diamond	Diamond	Zincblende	Wurtzite	Wurtzite	–
Band gap type	–	Indirect	Indirect	Direct	Direct	Direct	–
Lattice constant	a_0	–	–	–	3.191	3.112	Å
Lattice constant	c_0	5.431	5.646	5.653	5.185	4.982	Å
Bandgap energy	E_g	1.12	0.66	1.42	3.42	6.28	eV
Intrinsic carrier concentration	n_i	1.0×10^{10}	2.0×10^{13}	1.0×10^{6}	1.9×10^{-10}	1.0×10^{-34}	cm^{-3}
Effective DOS at CB edge	N_c	2.8×10^{19}	1.0×10^{19}	4.4×10^{17}	2.3×10^{18}	6.2×10^{18}	cm^{-3}
Effective DOS at VB edge	N_v	1.0×10^{19}	6.0×10^{18}	7.7×10^{18}	1.8×10^{19}	4.9×10^{20}	cm^{-3}
Electron mobility	μ_n	1500	3900	8500	1800	300	$cm^2/(Vs)$
Hole mobility	μ_p	450	1900	400	30	14	$cm^2/(Vs)$
Electron diffusion constant	D_n	39	101	220	39	7	cm^2/s
Hole diffusion constant	D_p	12	49	10	0.75	0.3	cm^2/s
Electron affinity	X	4.05	4	4.07	4.1	1.9	V
Breakdown field	V_{BR}	$\sim 3 \times 10^5$	$\sim 1 \times 10^5$	$\sim 4 \times 10^5$	$\sim 5 \times 10^6$	$\sim 1.5 \times 10^6$	V/cm
Minority carrier lifetime	τ	10^{-6}	10^{-6}	10^{-8}	10^{-8}	–	s
Electron effective mass	m_e^*	0.98 m_e	1.64 m_e	0.067 m_e	0.20 m_e	0.40 m_e	–
Heavy hole effective mass	m_{hh}^*	0.49 m_e	0.28 m_e	0.45 m_e	0.80 m_e	3.53 m_e	–
Relative dielectric constant	ε_r	11.9	16	13.1	8.9	8.5	–

A basic GaN transistor cross section is shown in Fig. 2.2. Fig. 2.3 shows the various polarization effects and resulting band diagram with 2-DEG. Creating a charge carrier channel in this fashion is termed *modulation doping,* so some refer to a transistor with this characteristic as a MODFET. In this paper we use the term HEMT. The contrast between GaN and Si in creating a FET charge carrier channel is easily seen, and although no intentional doping is required for GaN some processes use carbon or silicon as an n-type dopant in the AlGaN layer.

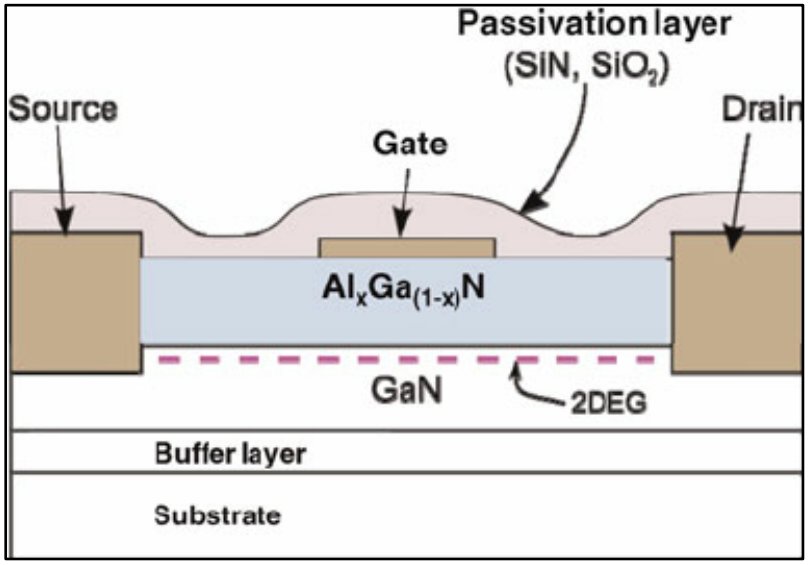

Fig. 2.2. Basic AlGaN/GaN transistor cross section [5].

Most GaN HEMTs are inherently depletion mode, or normally on, devices due to the 2-DEG and will conduct a drain-source current with a voltage is applied across those nodes unless the gate is held at a sufficiently negative voltage (pinch off). In RF applications, this detail is generally not a circuit design hindrance. However, for switching power electronics applications a complex gate drive circuit design is required to accommodate depletion mode GaN HEMTs. Adaptation of GaN for power electronics applications has spawned the innovation of enhancement mode, or normally off, GaN devices to allow simpler gate drive circuit design. This work focuses on depletion mode devices.

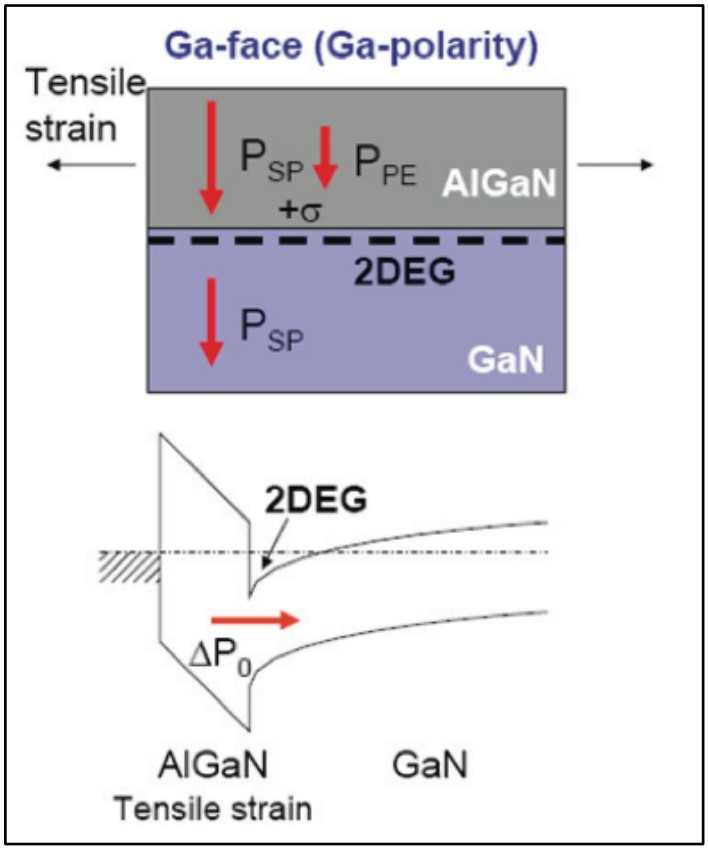

Fig. 2.3. AlGaN/GaN strain induced piezoelectric and spontaneous polarization components (top), and energy band diagram (bottom) [6].

Radiation Damage

There are two degradation mechanisms leading to cumulative radiation damage. One is total ionizing dose (TID), resulting from electron-hole pair creation where charge can become trapped and build up, producing an unwanted electric field. This can increase leakage currents, cause threshold voltage shifts and is a well understood phenomenon in silicon technology such as MOS where oxide and semiconductor layers interface. TID usually causes positive trapped charge in oxides, which result in the degradations described. Schottky-gate GaN-based HEMTs have no oxide layers between the gate and active region, making them less sensitive to TID than devices with gate dielectrics. Displacement damage is the other mechanism of interest in this

study. Displacement damage is generally caused by incident particles that disrupt the lattice. The results are degradation to charge carrier mobility, carrier number, threshold voltage, and leakage current. This effort is focused on displacement damage effects. The 1.8 MeV protons used for this study have a range in GaN of approximately 27 μm. Fig. 2.4 shows the Bragg curve (energy loss vs. depth) for this ion and target material. Energy is imparted to the target as the ion travels, and most is transferred at the Bragg peak, which is at the end of range. This is where the damage density will be highest.

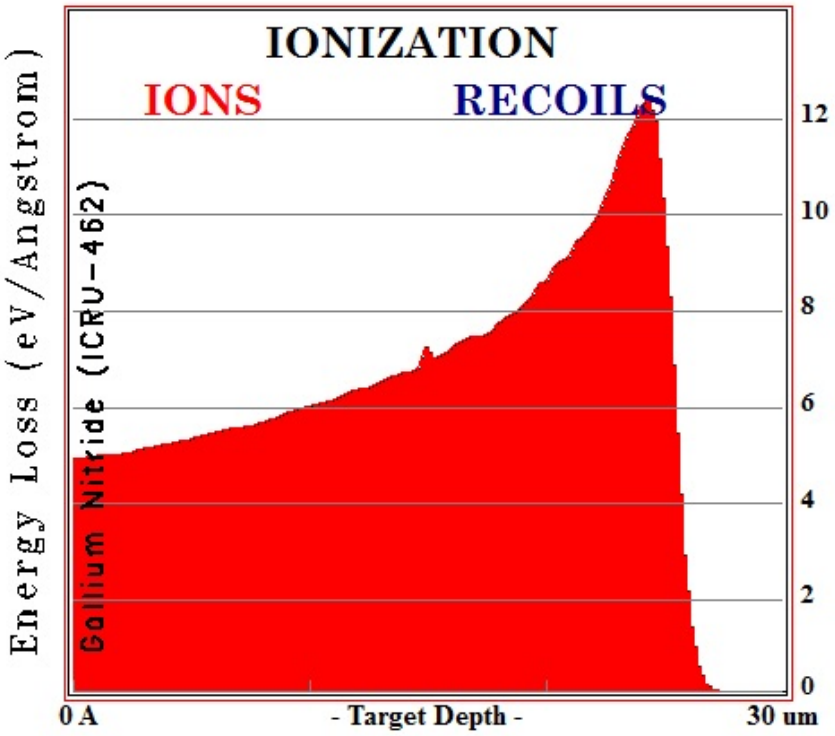

Figure 2.4. Bragg curve for 1.8 MeV protons in GaN.

CHAPTER 3

TEST SETUP

Devices

RF power devices from Cree (now Wolfspeed), RFMD (now Qorvo) and TriQuint (now Qorvo) were tested. Evaluation boards from the device manufacturers were used since they provided 50 ohm input and output matching networks. Three different operational modes were used during irradiation. Two devices were tested using each operational mode for a total of 18 parts tested. The semi-on (SO) mode was defined as a drain current of twice the value of the listed data sheet current at V_{TH} or approximately one tenth the drain current specified as I_{DQ} in the data sheet if a V_{TH} spec was not provided. The full-on (FO) mode was defined as operation at the I_{DQ} drain current data sheet specification but with no RF drive. The RF-on (RF) mode was defined as the FO mode with RF input drive. The RF input drive was provided at the mid-point frequency of the respective EVB's bandwidth. Basic device and EVB specifications and I_{DQ} for the operational modes are given in Table 3-1. Photos of the devices are in Fig. 3.1.

Table 3-1. Device and operational mode specs.

Vendor	Cree (now Wolfspeed)	RFMD (now Qorvo)	TriQuint (now Qorvo)
Model	CGH40120F	RF3934	T2G4005528
Max output power	120 W	120 W	55 W
Device bandwidth	DC - 2.5 GHz	DC - 3.5 GHz	DC - 3.5 GHz
EVB bandwidth	0.8 - 1.8 GHz (1 GHz)	2.11 - 2.17 GHz (60 MHz)	3.0 - 3.5 GHz (0.5 GHz)
V_{DD}	28 V	48 V	28 V
I_{DQ} (SO)	58 mA	40 mA	20 mA
I_{DQ} (FO, RF)	1.0 A	0.44 A	0.20 A

Fig. 3.1. Device photos.

Thermoelectric Cooling

A thermoelectric (TE), or Peltier, cooling system was assembled for this effort in order to keep the device under test (DUT) as close to a constant temperature as possible. The system components are listed in Table 3.2.

Table 3.2. TE system components.

Quantity	Model	Function	Manufacturer
4	VT-199-1.4-0.8	thermoelectric module	TE Technology, Inc.
1	LC-SSX1	heat exchanger	TE Technology, Inc.
1	TC-48-20	TE cooler temperature controller	TE Technology, Inc.
1	MP-3193	thermistor	TE Technology, Inc.
1	PS-24-20	24 V, 20 A power supply	TE Technology, Inc.
1	EXC-800	water chiller	Koolance, Inc.
n/a	641-EV	high vacuum compatible thermal grease	Aremco Products, Inc.

Four TE modules were mounted between the heat exchanger and a 0.25 inch thick aluminum plate. Shallow recesses were milled into the heat exchanger and aluminum plate to keep the modules captive. The plate was drilled and tapped to accommodate the three EVBs. Slots to embed half of the thermistor were milled in the center of the outer side of the plate and the back of each EVB. This positioned the thermistor under the DUT, separated from it by 0.25 inch of EVB base metal, for temperature sensing. The back of the heat exchanger was drilled and

tapped for a test chamber stage mounting bracket. Liquid and electrical chamber feedthroughs supply the TE system. Vacuum compatible thermal grease was applied to all mating surfaces. Fig. 3.2 shows progressive assembly of the TE system.

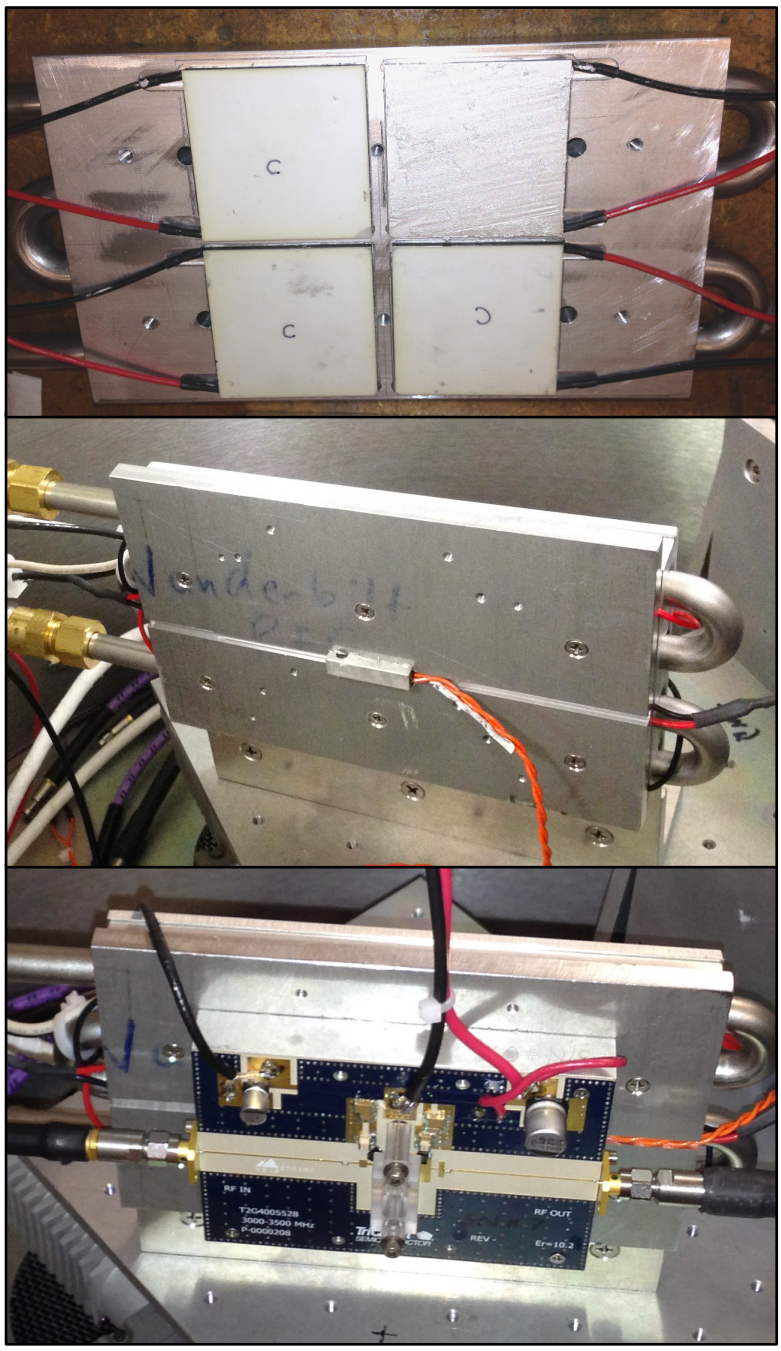

Fig. 3.2. TE system assembly.

The TC-48-20 temperature controller uses the MP-3193 thermistor for temperature input. The PS-24-20 powers the controller as well as provides power to its pulse width modulation (PWM) TE module drive output. Temperature set point, proportional bandwidth, integral gain and derivative gain are the adjustable control parameters. The LC-SSX1 heat exchanger is capable of removing 300 watts of heat and each TE module will remove around 140 watts of heat. As assembled, the system will readily maintain a thermocouple temperature of 20 °C with a 150 watt heat load and 22 °C chilled water flowing in the heat exchanger at 2 liters/minute. In practice the thermistor read 20 °C ±0.2 °C during all testing.

Test Equipment and Protocol

The following table lists the major equipment used for this effort.

Table 3.3. List of equipment.

National Electrostatics Corp 6SDH Pelletron Accelerator
Agilent B1505A Power Device Analyzer
Agilent N5245A PNA-X Microwave Network Analyzer
Agilent E8257D PSG Analog Signal Generator
Tektronix RSA51246A Signal Analyzer
Fairview Microwave SBBA-060-44-01-SMA RF amplifier
RF Lambda RFS-150GXA 40 dB 150 W fixed attenuator

The Vanderbilt Pelletron [8] provided 1.8 MeV protons at an average flux of approximately $3x10^{10}$ protons/(cm^2·s). Rutherford backscattered protons from a 120 nm thick gold foil in the beam path were used for real-time dosimetry. The foil also scatters the beam making it more uniform downstream. A plate with a one inch diameter aperture vignettes the beam so that the exposure area is approximately that same size. A 1/8 inch thick lead shield with

a 3/8 inch aperture was used directly in front of the DUT to ensure only the DUT was exposed and nothing else on the EVB. Fig. 3.3 is a photo of the shield in front of the RFMD EVB.

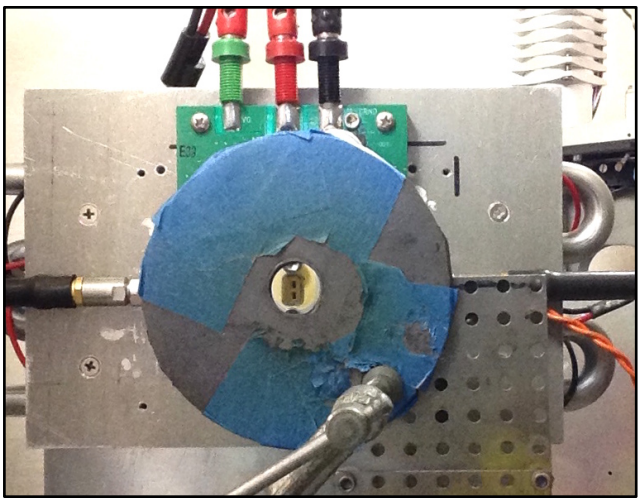

Fig. 3.3. EVB shield

Anti-static/ESD wrist strap and smock were worn during handling of devices, changing cable configurations between tests, and running electrical tests. The devices were de-lidded by carefully heating on a grounded aluminum plate and pulling the lids off with tweezers. The EVB was first mounted on the TE system and then the DUT to the EVB using the plastic retainers. EVB chamber feedthrough connections consisted of DC gate and drain lines using a common source line and RF input and output coaxial connections. After vacuum pump-down, pre-irradiation tests were conducted. DC parametric tests were conducted first using the B1505A connected to the gate and drain feedthroughs and 50 ohm loads on the RF input and output feedthroughs. Next was S-parameter testing with the N5245A. The 50 ohm loads were removed from the feedthroughs and the N5245A was connected. The B1505A gate and drain feedthrough connections were removed and replaced with connections from adjustable DC power supplies. The gate voltage was initially set to -5 V to ensure the DUT powers up in the off state. Then, as

given in Table 3.1 for the installed device type, the drain voltage was set to the appropriate V_{DD} value and subsequently the gate voltage was raised until the listed I_{DQ} value for the FO bias condition was attained. S-parameter measurements were then conducted with the N5245A. The DC drain voltage was reduced to zero and then the same done to the gate voltage. The RF cables were moved from the N5245A to the E8257D signal generator and RSA51246A analyzer. After restoring DC gate and drain drive the power RF measurements were made using the RSA51246A, E8257D, Fairview RF amplifier and RF Lambda attenuator. Preparing for irradiation, the appropriate RF connections depending on the required bias (50 ohm load or RSA51246A and E8257D) were made. Then DC gate and drain voltages appropriate for the operational mode (SO, FO, RF) were established followed by RF drive if the RF operational mode was used. The DUT was irradiated to the first fluence step and then the entire process repeated to get the post-rad measurements. Consecutive iterations followed with the fluence steps incremented accordingly, ending with the maximum irradiation fluence and measurements. The fluence levels are listed in Table 3.4 and the measurement test setup is shown in Fig. 3.4.

Table 3.4. Irradiation fluence steps.

Step	Fluence, H^+/cm^2
Pre	0
1	1×10^{12}
2	3×10^{12}
3	1×10^{13}
4	3×10^{13}
5	1×10^{14}

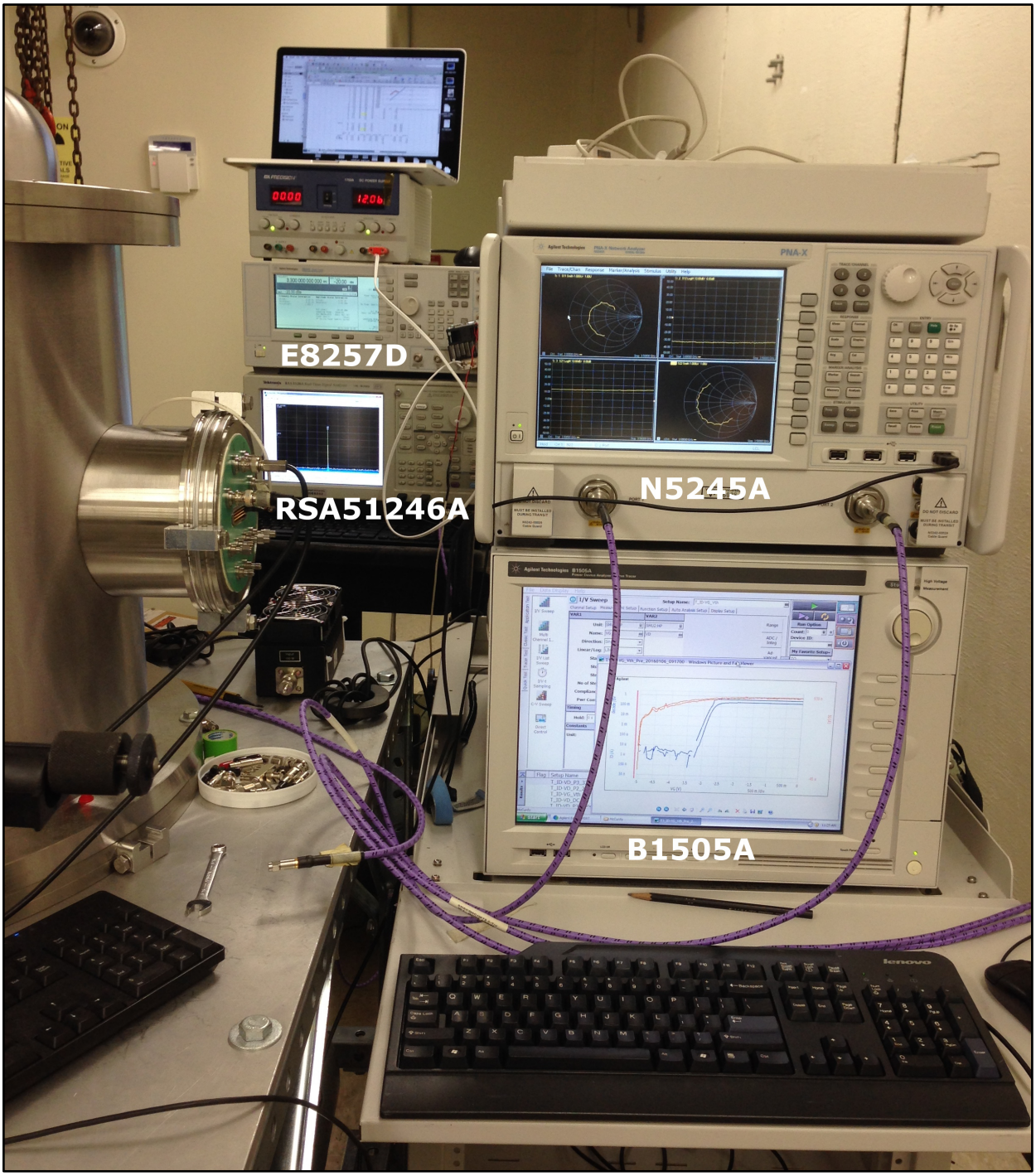

Fig. 3.4. Test equipment setup.

S-parameters and the Smith Chart

S-parameters are a measure of RF performance at specific frequencies in the linear regime of active device operation in a controlled impedance system. The controlled impedance for the devices and EVBs of this study is 50 ohms. To insure linear regime operation the N5245A PNA-X Microwave Network Analyzer RF output level at the DUT was -16 dBm, or approximately 25 microwatts. This included cabling losses. Transmission and reflection of RF voltage signals at the ports comprise the phenomenon characterized. Fig. 3.5 shows the topology with signal propagation directions.

Fig. 3.5. Two-port network topology.

Equations (1), (2), (3) and (4) below define the four two-port S-parameters as ratios of the various combinations of input and output voltage signals, a_x and b_x, respectively, with the output terminated in a matched load and no signal into the unused input. The first subscript of the S-parameter designator is the output port and the second is the input port. Forward and reverse transmission S-parameters, S_{21} and S_{12}, respectively, are generally displayed on a rectangular plot, similar to a Bode plot, with response in dB shown on the ordinate and frequency on the abscissa. Forward and reverse reflection coefficient S-parameters, S_{11} and S_{22}, respectively, are generally displayed on a Smith chart.

$$S_{11} = \left.\frac{b_1}{a_1}\right|_{a_2 = 0}$$ Forward reflection coefficient, output terminated with matched load. (1)

$$S_{21} = \left.\frac{b_2}{a_1}\right|_{a_2 = 0}$$ Forward transmission gain, output terminated with matched load. (2)

$$S_{12} = \left.\frac{b_1}{a_2}\right|_{a_1 = 0}$$ Reverse transmission gain, output terminated with matched load. (3)

$$S_{22} = \left.\frac{b_2}{a_2}\right|_{a_1 = 0}$$ Reverse reflection coefficient, output terminated with matched load. (4)

The Smith chart, invented by Phillip H. Smith, is a versatile tool for graphically displaying and calculating many RF parameters [17]. It is commonly used to display the forward (or reverse) reflection coefficient in terms of the input (or output) impedance it represents and how closely that impedance matches the system impedance, in this case 50 ohms resistive. The chart represents the complex reflection coefficient plane in terms of normalized impedance. It is made up of constant resistance and constant reactance circles. A simplified chart is shown in Fig. 3.6. All the circles have a common point that is the point on the right side of the chart at the 3 o'clock position. This point represents infinite impedance. The zero resistance point is diametrically across on the left side of the chart at the 9 o'clock position. Circles of constant resistance extend to the left from the common point, getting progressively larger in diameter until the zero resistance circle is formed. Constant positive, or inductive, reactance circles extend upward from the common point with increasing diameter and constant negative, or capacitive, reactance circles extend downward. Since the Smith chart is a normalized system it can be used with any controlled impedance network, whether 50 ohm, 75 ohm, etc. The center point of the Smith chart represents the normalized complex impedance 1.0 + *j*0. That point represents the

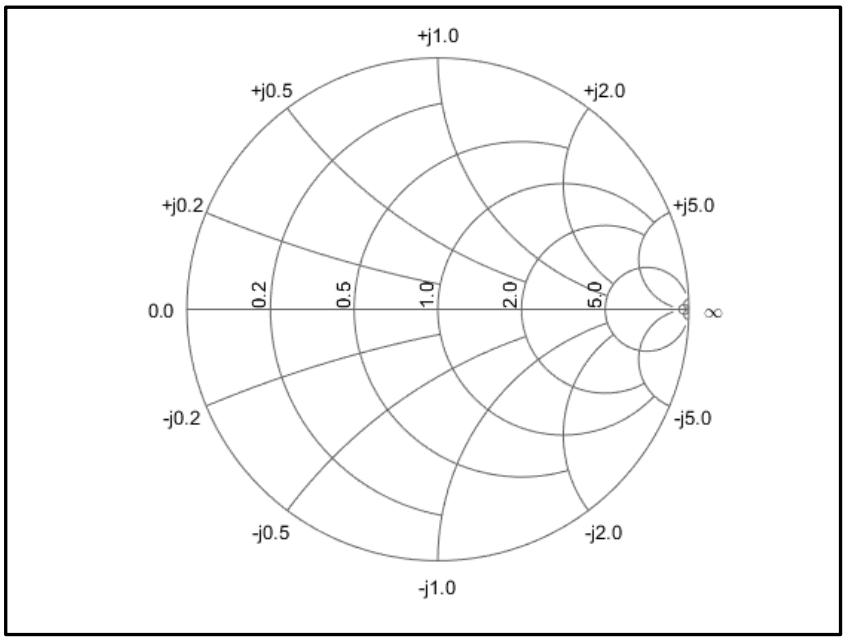

Fig. 3.6. Simplified Smith Chart showing constant resistance and reactance circles.

controlled impedance of the system, 50 ohms resistive as previously stated. So we can multiply any point on the chart by the controlled system impedance to get the actual impedance represented by that point. If the reflection coefficient point is at chart center then that port is perfectly matched and there is zero reflection. As the reflection coefficient point moves radially outward toward the circumference then the reflection coefficient tends toward 1, and the signal is fully reflected in the limit.

CHAPTER 4

RESULTS

DC parameters

The I_D-V_G DC measurements were the first to be performed during the measurement phase. The gate voltage was swept from -5.0 V to 0 V at drain voltages of 0.01 V and 0.1 V. The data from the V_D = 0.1 V set was used for these analyses. The transconductance, g_m, was taken as the maximum slope of the I_D-V_G curve. The threshold voltage, V_{TH}, was taken as the point where the I_D-V_G curve maximum slope line intersected the V_G axis. Fig. 4.1 shows these parameters graphically using a black line tangent to the maximum slope on the I_D-V_G maximum fluence curve for C4 (SO). The two parameters were calculated using the respective curve data. For comparison there is a magenta line tangent to the maximum slope of the pre-irradiation curve showing a greater slope, or higher g_m, and lower V_{TH}. All intermediate response curves are also shown.

Fig. 4.2 shows the maximum V_{TH} shift and g_m degradation responses for all devices. Two TriQuint parts that failed during testing are noted with yellow highlighting. Increasing shift and degradation are toward the right, with worst case at +0.4 V V_{TH} shift and 30% g_m degradation. The general susceptibility trend from least to most by manufacturer was Cree, RFMD, TriQuint. There does not appear to be a susceptibility trend with operational mode.

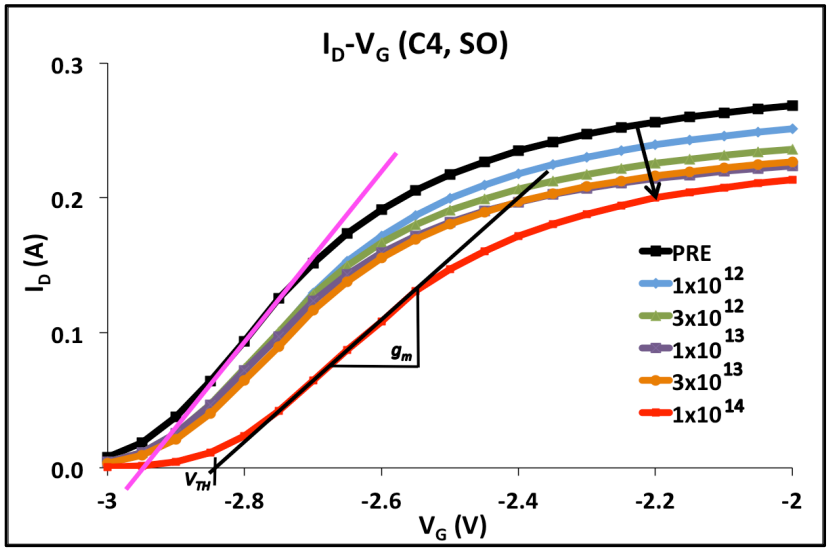

Fig. 4.1. I_D-V_G Curves for C4 (SO) showing V_{TH} and g_m calculations.

	FO C8	SO C10	RF C5	FO C9	RF C2	SO C4	SO T12	FO T13	RF R8	FO R6	SO R5	FO R7	RF T16	SO R4	SO T11	FO T14	RF T15	RF R9
V_{TH} shift, V	-0.070	0.066	0.103	0.103	0.104	0.105	0.169	0.294	0.312	0.325	0.327	0.367	0.368	0.369	0.377	0.379	0.385	0.409
	RF C2	FO C8	SO C10	RF T15	RF C5	FO T13	FO C9	SO R5	SO T12	FO R7	SO R4	RF R8	RF R9	FO T14	RF T16	FO R6	SO T11	SO C4
g_m degr	0.980	0.957	0.950	0.934	0.903	0.903	0.903	0.899	0.896	0.857	0.856	0.845	0.791	0.790	0.787	0.774	0.717	0.715

Fig. 4.2. Maximum V_{TH} shift and g_m degradation. Color indicates manufacturer, operational mode listed as well as DUT serial number. T12 and T13 failed before ultimate fluence.

Fig. 4.3 shows the V_{TH} shift for all DUTs grouped by operational mode with ±1 standard deviation error bars. The initial V_{TH} shift of C8 (FO) at 10^{12} fluence is likely anomalous as it went negative by approximately 0.1 V. That was the only part to demonstrate a negative V_{TH} shift on the first fluence step. Thus the error bars for the Cree (FO) devices are large. All other devices had positive V_{TH} shifts on the initial irradiation step. The data for that test pair, C8 and C9, is shown in Fig. 4.4 and demonstrates that, aside from the initial step response, the two response plots are very similar. They both trend slightly in the negative direction until the ultimate fluence point which jumps noticeably in the positive direction.

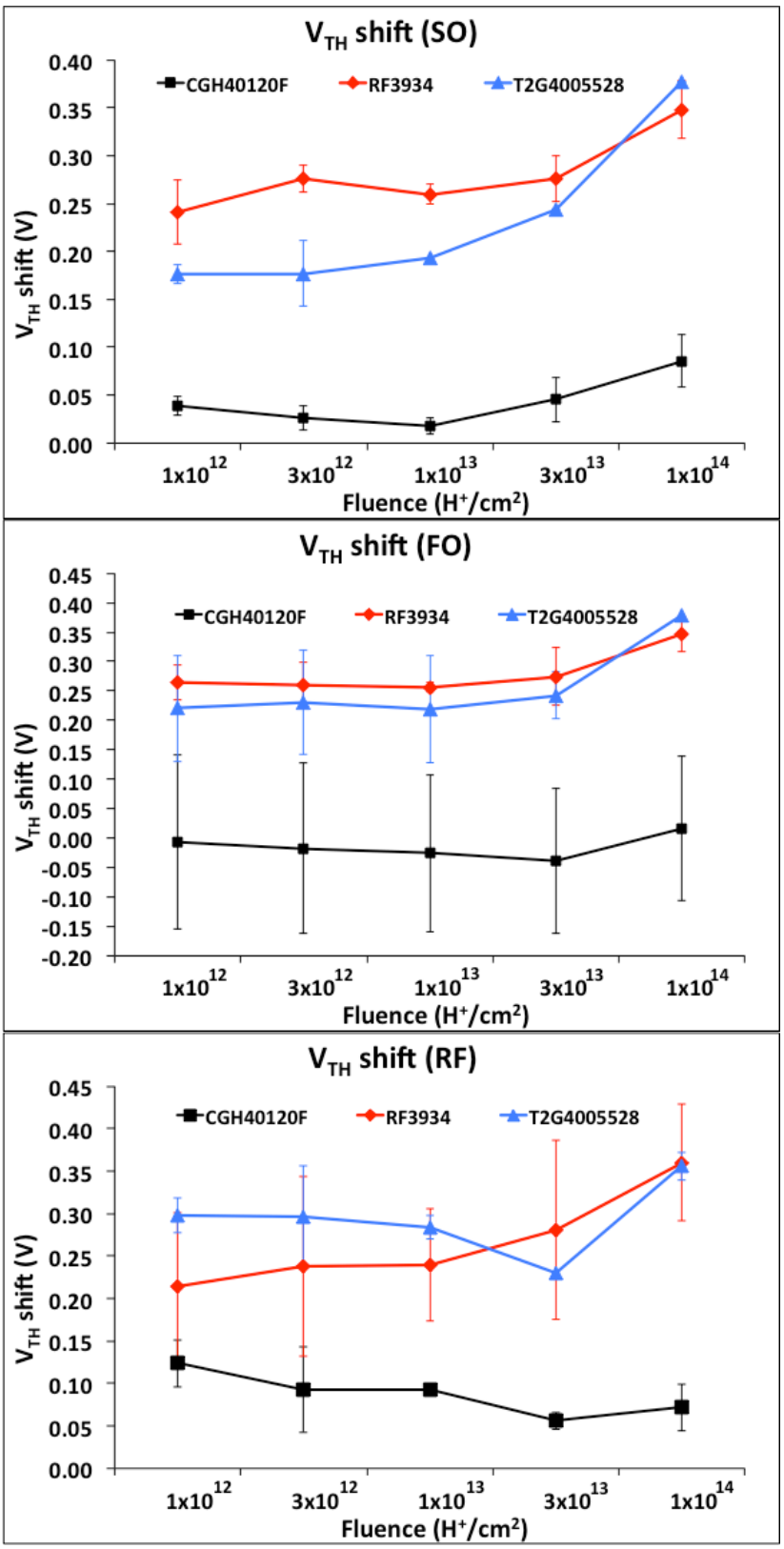

Fig. 4.3. V_{TH} shift for all operational modes: SO - top, FO - mid, RF - bottom.

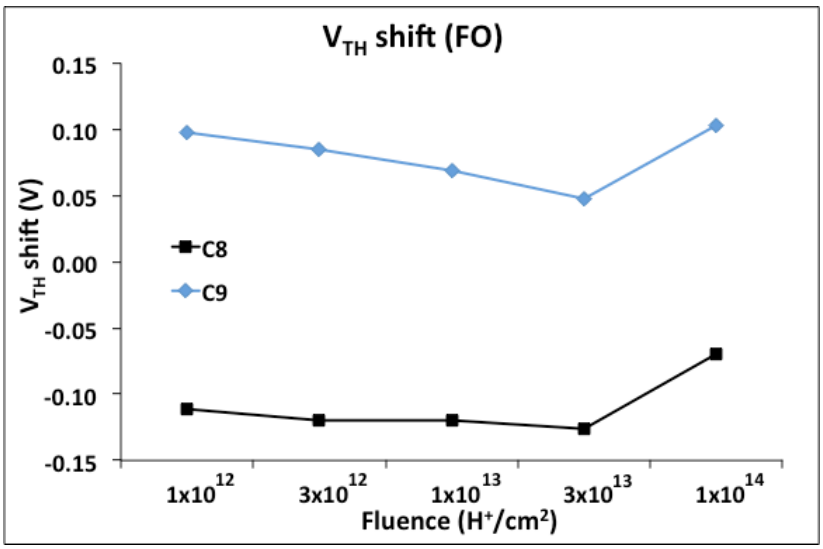

Fig. 4.4. CGH40120F (FO) V_{TH} shift

The RFMD and TriQuint V_{TH} shift (RF) plots in Fig. 4.3 are rather noisy, as evidenced by the ±1 standard deviation error bars and the TriQuint (RF) zigzag curve shape. The cause of these anomalies is not clear but is believed to be due to a non-catastrophic ESD-like event, even with the grounding precautions taken, that occurred during one of the multiple test cable change operations. Ignoring the anomalies, the shape of the individual curves for the two devices under each operational mode are similar. The curves for the (SO) condition appear to have a more pronounced increase with fluence than the (FO) and (RF) conditions.

Fig. 4.5 displays the Cree (SO) individual g_m degradation plots clearly showing that C4 has the worst case g_m degradation as listed in Fig. 4.2. Other g_m degradation responses are shown in Fig. 4.6 with TriQuint (FO) parts (top) being a typical example. The CREE (FO) (mid) and (RF) (bottom) parts showed slight transconductance increase after the first fluence step. The increase largely persisted until the last fluence step in the (RF) case. This phenomenon has previously been demonstrated to be due to defect dehydrogenation [12].

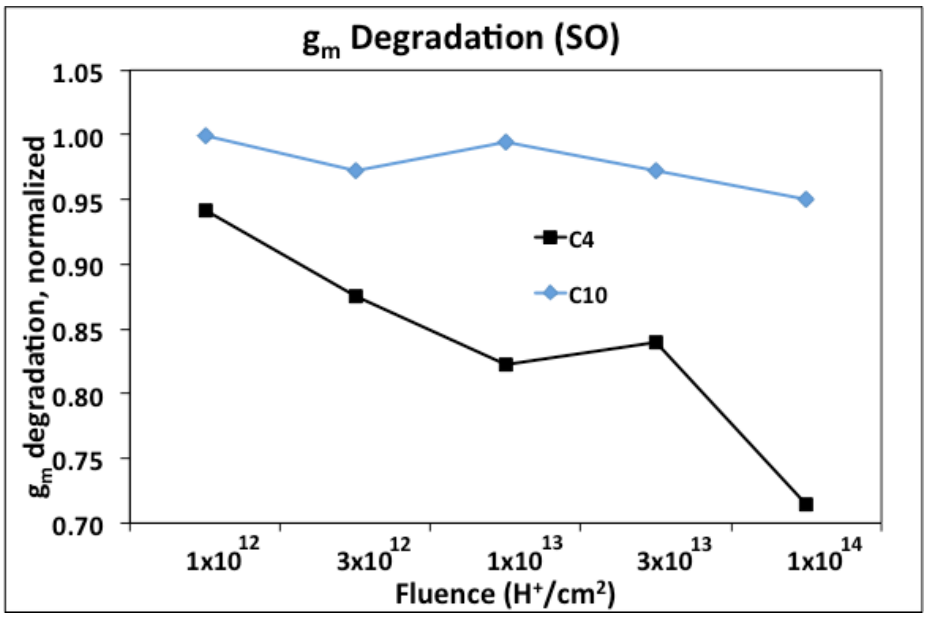

Fig. 4.5. C4 and C10 (SO) g_m degradation

Small Signal RF

S-parameter measurements followed the DC tests. The Cree parts showed very low S-parameter degradation over the entire exposure range. They had the following maximum *S21* deviation from pre-irradiation values at the EVB center frequency of 1.3 GHz: (SO) ±0.25 dB, (FO) ±0.07 dB, (RF) ±0.15 dB. The RFMD parts were slightly softer to protons showing a maximum *S21* degradation of approximately -0.4 dB. The C4 (SO) and R8 (RF) *S21* responses over their EVB frequency measurement ranges are shown in Fig. 4.7.

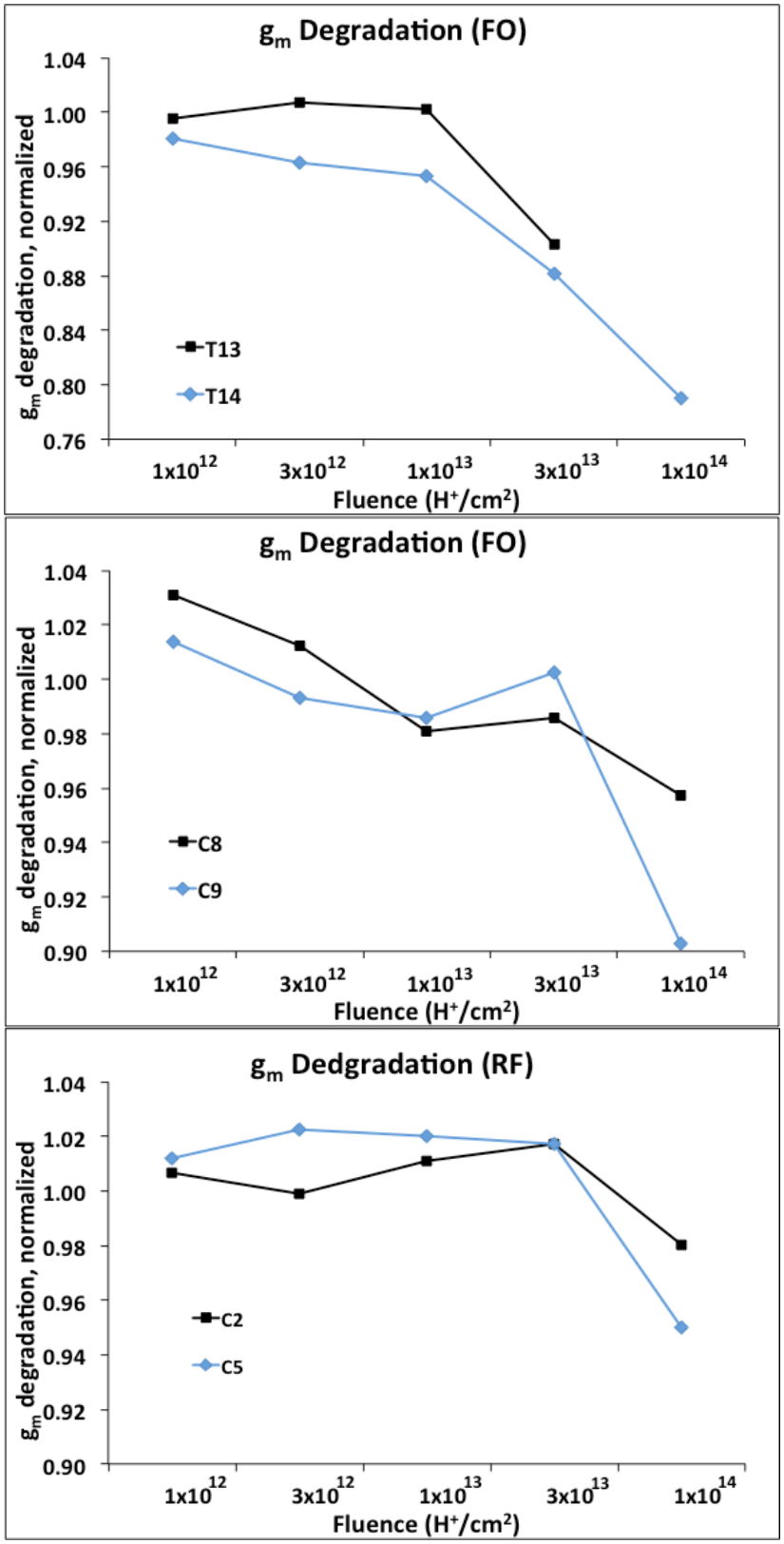

Fig. 4.6. Typical g_m degradation for most devices (top); Cree (FO) (mid) and (RF) (bottom) with the latter showing persistent increase in g_m until last fluence step.

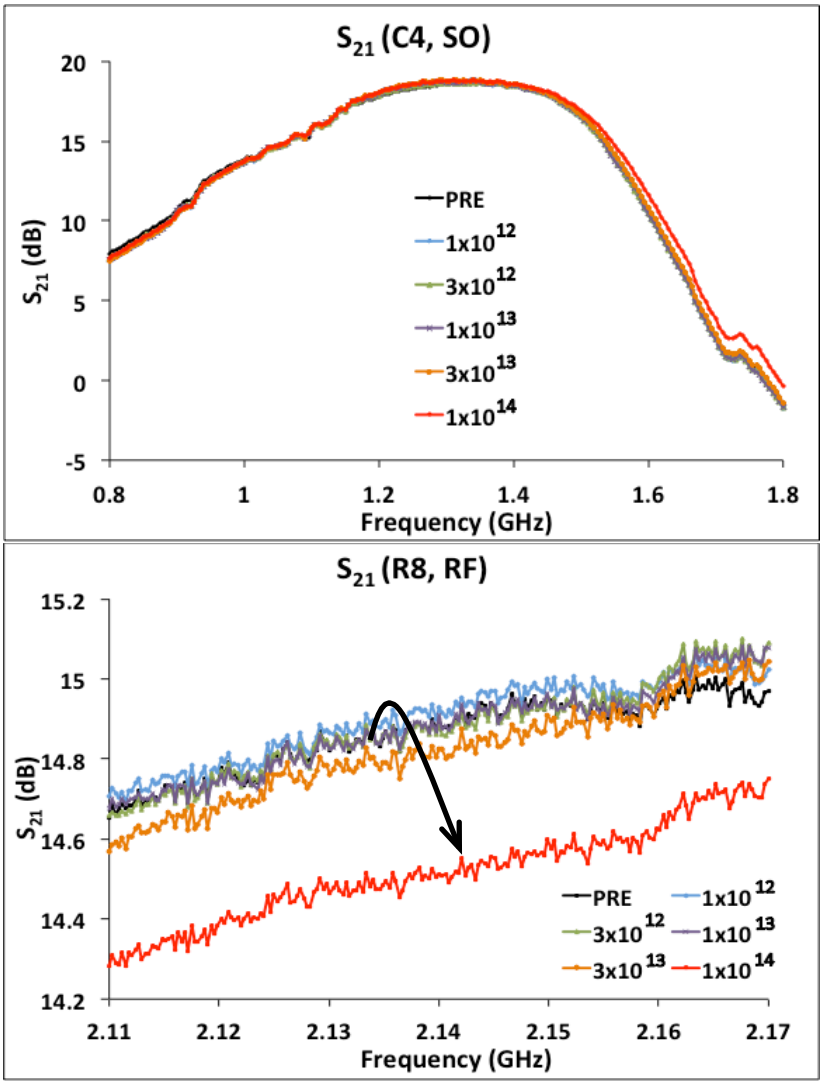

Fig. 4.7. S_{21} response: C4 (SO) (top), R8 (RF) (bottom) .

It is interesting to note the slight improvement in the RFMD *S21* response before it degrades at higher fluence. *S11* monotonically improved as much as 1.5 dB for these parts and was typical for these devices. The TriQuint parts show a more marked improvement in all S-parameters except *S22* with fluence. Fig. 4.7 and Fig 4.8 show the responses. The lower *S11* indicates better impedance matching and may at least partly explain the increase in *S21*. If more signal is input due to better impedance matching then more is available to amplify, which shows

up as an increase in *S21*. The protons produced changes in the GaN material properties that can be seen in Fig. 4.9, especially the *S11* plots which are the Smith charts in the upper left in each quad. The upper quad is pre-irradiation and the lower quad is post max fluence of 10^{14} p^{+}/cm^{2}. The shape of the trace is dramatically different between the two and the latter is closer to the chart center demonstrating better impedance matching.

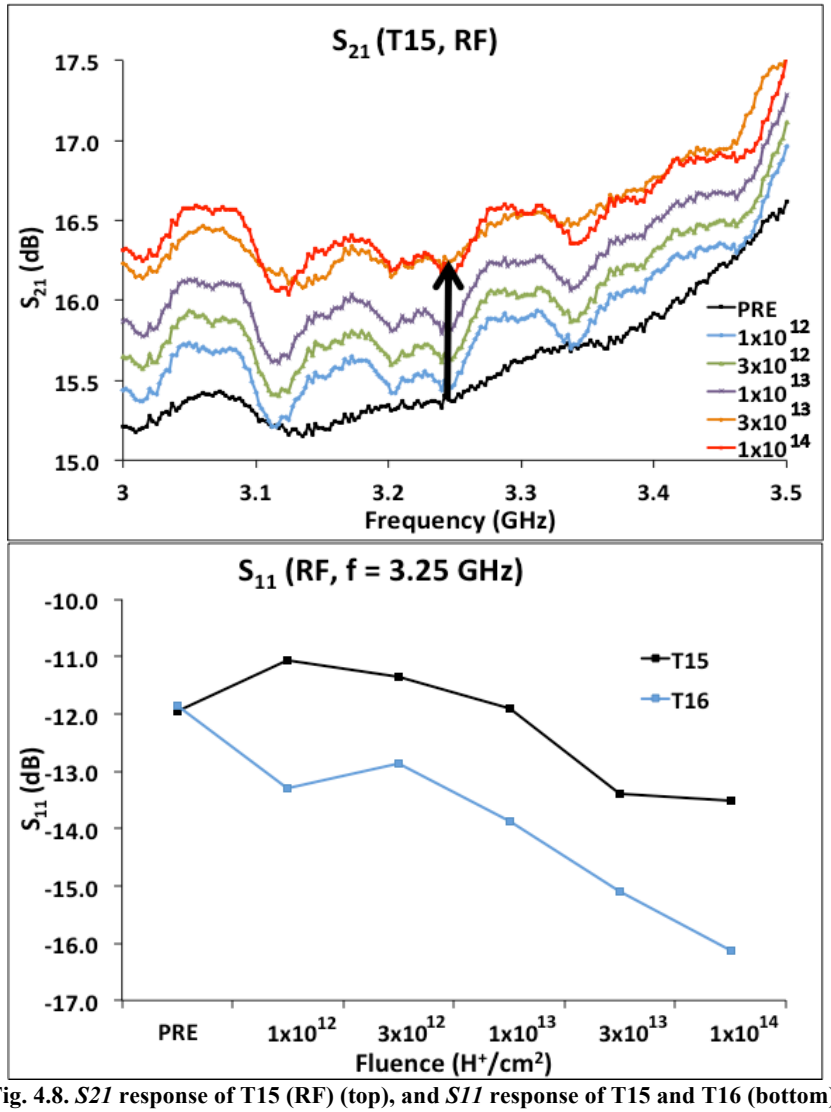

Fig. 4.8. *S21* response of T15 (RF) (top), and *S11* response of T15 and T16 (bottom).

Recall the shield used in front of the DUT EVBs (Fig. 3.3) so that only the GaN devices were irradiated. Any impedance changes must be in the semiconductor and not in the various passives

on the EVB. Note the *S21* improvement in the lower left plots in each quad. Almost 2 dB of improvement can be seen. The *S22* Smith charts (reverse reflection, lower right in each quad) show slight degradation in that the trace of the post-rad is a little further from the chart center. *S12* (reverse transmission, upper right in each quad) improved by as much as 3.5 dB. Some of the performance improvements, especially *S21*, may be due to enhancement of any or all of the 2DEG carrier mobility, density, or depth. They suffer worse DC parametric effects but increased small signal RF gain.

Large Signal RF

The Cree devices were driven by a 19 dBm RF signal, or approximately 80 milliwatts. The amplified output was 4 watts. This relatively low level was due to the fact that the Fairview Microwave amplifier's specified bandwidth was 2 GHz to 6 GHz. The Cree RF large signal power mode was driven at the EVB mid-frequency which was 1.3 GHz, enough below the Fairview amplifier's full bandwidth to prevent the Cree parts from being driven to the level the other parts were. RFMD and TriQuint parts were driven by a little over 1 watt at their respective EVB mid-frequencies and they exhibited RF output power of 30 watts.

Cree devices showed a maximum 0.42 dB gain change for large signal RF operation over all irradiation bias conditions. The RFMD devices exhibited a maximum of 0.15 dB change and the TriQuint devices showed as much as 0.7 dB gain in RF large signal response during the irradiation but decreased at the last proton dose considered here. Fig.4.10 shows plots of the worst case large signal RF gain responses for each manufacturer. The plots are on the same vertical scale for comparison purposes.

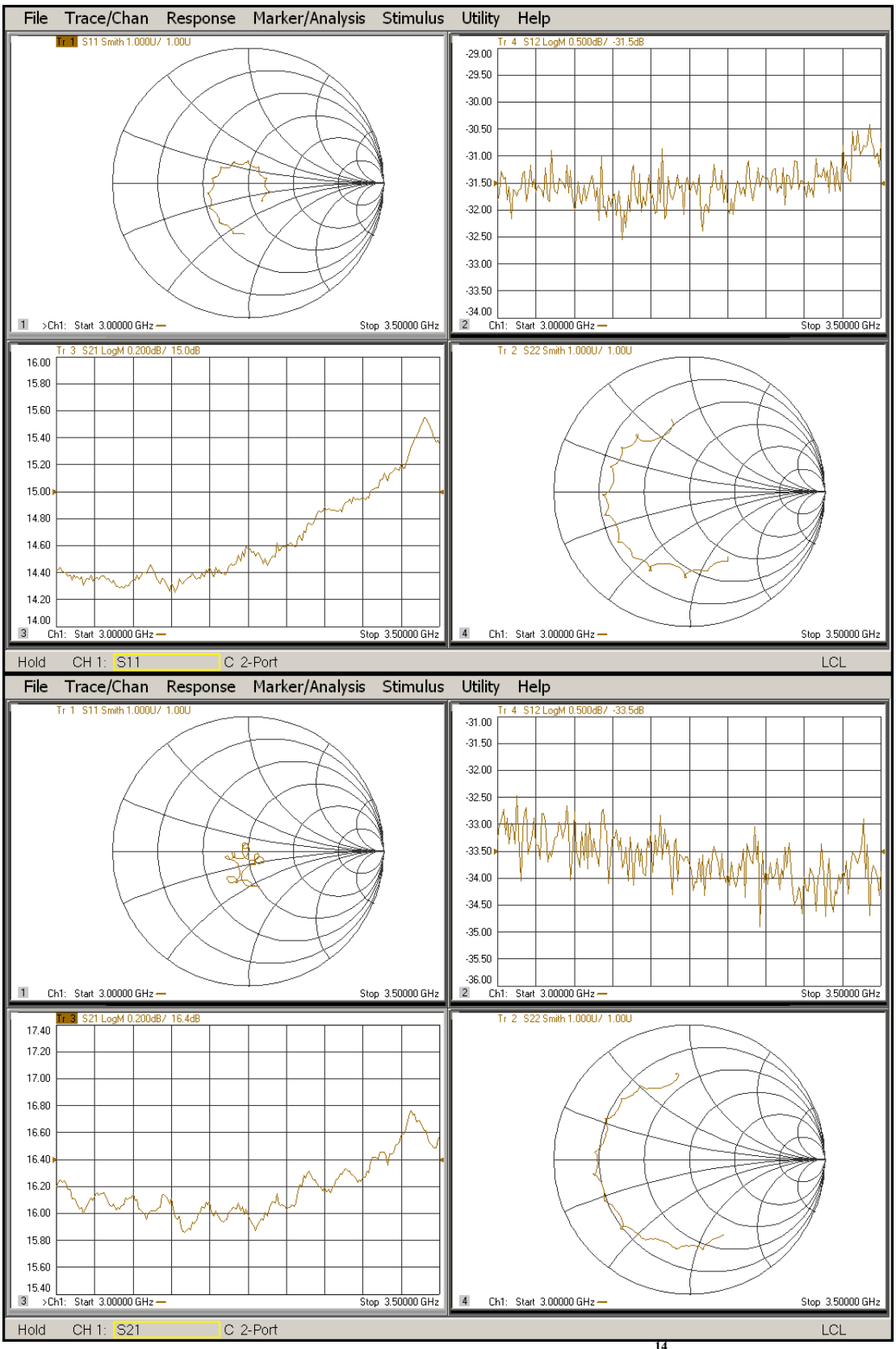

Fig. 4.9. T11 (SO) S-parameter sweeps pre-irradiation (top) and 1x10^{14} fluence (bottom).

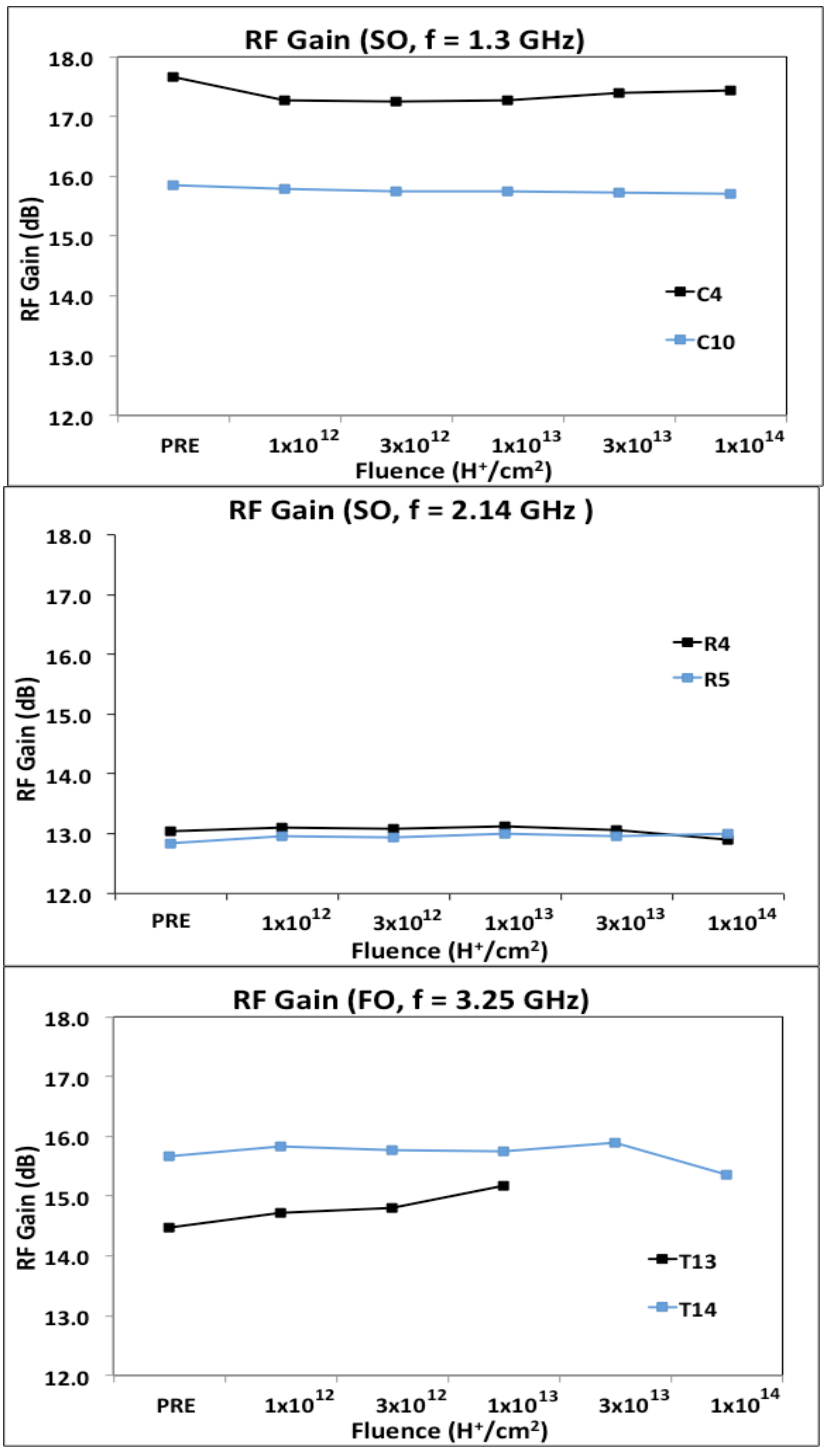

Fig. 4.10. RF large signal gain, worst cases

CHAPTER 5

CONCLUSIONS

Radiation effects testing data collection is usually a compromise between making efficient use of time and getting enough of the right data. This particular work would inform future efforts to take DC parametric measurements over a narrower V_G range and with smaller steps in order to reduce noise in the V_{TH} and g_m calculations.

Another radiation effects testing compromise involves the number of devices available for test. To eliminate any ESD-induced or other handling related anomaly due to cable changes it would be advised to have a highly robust cabling change system. This could conceivably be implemented with various types of DC and RF high fidelity relays arranged in an appropriate matrix. One challenge would probably be finding relays with sufficient power handling capacity. Such an arrangement would allow response correlation across multiple electrical parameters for each DUT. The alternative of having sufficient number of parts on hand so that only one type of electrical test is conducted on a given part would preclude this but would reduce the opportunity for ESD effects.

Future RF power testing should be done with appropriate RF drive power levels to attain the DUT RF output power levels that each part type is rated. The input drive level would need to be carefully planned in terms of adequate bandwidth and power level. Even if the RF power test signal to the DUT is from an amplifier operating into compression any harmonics in that signal should be adequately filtered by the EVB input network.

Semiconductor manufacturers often do not reveal much about their device manufacture due to the highly proprietary nature of process development. Knowledge of device processing then may not be available to be applied to predict certain responses based on previous tests of devices of known processes. The rate of process changes as the technology matures is high. Thorough testing of candidate devices should be done to ensure margins are met and performance will be within expected limits. Relying on prior test data of seemingly similar parts is not an option for applications with high reliability requirements.

REFERENCES

[1] E. S. Yang, *Fundamentals of Semiconductor Devices*, New York: McGraw-Hill, 1978.

[2] R. F. Pierret, *Advanced Semiconductor Fundamentals*, 2nd Ed., New Jersey: Prentice Hall, 2003.

[3] H. Morkoç, *Nitride Semiconductor Devices: Fundamentals and Applications*, Weinheim, Germany: Wiley-VCH, 2013.

[4] P. Hehenberger, Ph.D. Dissertation, Vienna University of Technology, Dec. 2011.

[5] S. Piotrowicz, E. Morvan, R. Aubry, G. Callet, E. Chartier, C. Dua, J. Dufraisse, D. Floriot, J.-C. Jacquet, O. Jardel, Y. Mancuso, B. Mallet-Guy, M. Oualli, Z. Ouarch, M.-A. Poisson, N. Sarazin, M. Stanislawiak, and S. L. Delage, "Overview of AlGaN/GaN HEMT technology for L- to Ku-band applications," *International Journal of Microwave and Wireless Technologies*, vol. 2, no. 1, pp. 105–114, Feb. 2010.

[6] M. Lindeborg, "Surface morphology and electrical properties of GaN layers," *The Harvard Undergraduate Research Journal*, vol. 3, no. 2, pp. 1–16, Jan. 2011.

[7] F. Sacconi, A. Di Carlo, P. Lugli, and H. Morkoç, "Spontaneous and piezoelectric polarization effects on output characteristics of AlGaN/GaN HEMTs," *IEEE Trans. Electron Devices*, vol. 48, no. 3, pp. 450–457, Mar. 2001.

[8] M. W. McCurdy, M. H. Mendenhall, R. A. Reed, B. R. Rogers, R. A. Weller, and R. D. Schrimpf, "Vanderbilt Pelletron — Low energy protons and other ions for radiation effects on electronics," in *Proc. IEEE Radiat. Effects Data Workshop*, Boston, MA, USA, Jul. 2015, pp. 146–151.

[9] J. Chen, E. X. Zhang, C. X. Zhang, M. W. McCurdy, D. M. Fleetwood, R. D. Schrimpf, S. W. Kaun, E. C. H. Kyle, and J. S. Speck, "RF performance of proton-irradiated AlGaN/GaN HEMTs," *IEEE Trans. Nucl. Sci.*, vol. 61, no. 6, pp. 2959–2964, Dec. 2014.

[10] R. Jiang, E. X. Zhang, M. W. McCurdy, J. Chen, X. Shen, P. Wang, D. M. Fleetwood, R. D. Schrimpf, S. W. Kaun, E. C. H. Kyle., J. S. Speck, and S. T. Pantelides, "Worst-case bias for proton and 10-keV X-ray irradiation of AlGaN/GaN HEMTs," *IEEE Trans. Nucl. Sci.*, vol. 64, no. 1, pp. 218–225, Jan. 2017.

[11] A. Sasikumar, Z. Zhang, P. Kumar, E. X. Zhang, D. M. Fleetwood, R. D. Schrimpf, P. Saunier, C. Lee, S. A. Ringel, and A. R. Arehart, "Proton irradiation-induced traps causing V_T instabilities and RF degradation in GaN HEMTs," *Proc. IEEE Intl. Rel. Phys. Symp. (IRPS)*, pp. 2E.3.1–2E.3.6, Apr. 2015.

[12] J. Chen, Y. S. Puzyrev, C. X. Zhang, E. X. Zhang, M. W. McCurdy, D. M. Fleetwood, R. D. Schrimpf, S. T. Pantelides, S. W. Kaun, E. C. H. Kyle, and J. S. Speck, "Proton-induced dehydrogenation of defects in AlGaN/GaN HEMTs," *IEEE Trans. Nucl. Sci.*, vol. 60, no. 6, pp. 4080–4086, Dec. 2013.

[13] T. Roy, E. X. Zhang, Y. S. Puzyrev, D. M. Fleetwood, R. D. Schrimpf, B. K. Choi, A. B. Hmelo, and S. T. Pantelides, "Process dependence of proton-induced degradation in GaN HEMTs," *IEEE Trans. Nucl. Sci.*, vol. 57, no. 6, pp. 3060–3065, Dec. 2010.

[14] N. E. Ives, J. Chen, A. F. Witulski, R. D. Schrimpf, D. M. Fleetwood, R. W. Bruce, M. W. McCurdy, E. X. Zhang, and L. W. Massengill, "Effects of proton-induced displacement damage on GaN HEMTs in RF power amplifier applications," *IEEE Trans. Nucl. Sci.*, vol. 62, no. 6, pp. 2417–2422, Dec. 2015.

[15] J. Chen, Y. S. Puzyrev, E. X. Zhang, D. M. Fleetwood, R. D. Schrimpf, A. R. Arehart, S. A. Ringel, S. W. Kaun, E. C. H. Kyle, J. S. Speck, P. Saunier, C. Lee, and S. T. Pantelides, "High-field stress, low-frequency noise, and long-term reliability of AlGaN/GaN HEMTs," *IEEE Trans. Device Mater. Reliab.*, vol. 16, no. 3, pp. 282–289, Sep. 2016.

[16] S. Mukherjee, Y. Puzyrev, J. Chen, D. M. Fleetwood, R. D. Schrimpf, and S. T. Pantelides, "Hot-carrier degradation in GaN HEMTs due to substitutional iron and its complexes," *IEEE Trans. Electron Devices*, vol. 63, no. 4, pp. 1486–1494, Apr. 2016.

[17] P. H. Smith, *Electronic Applications of the Smith Chart*, 2nd Ed., SciTech, Raleigh, N.C.: SciTech, 2006, pp. 27–44